Lab on a Chip

Accepted Manuscript

ROYAL SOCIETY OF CHEMISTRY

www.rsc.org/loc

A numerical simulation setup to predict the motion of arbitrarily shaped particles under the simultaneous effects of streaming and radiation forces.

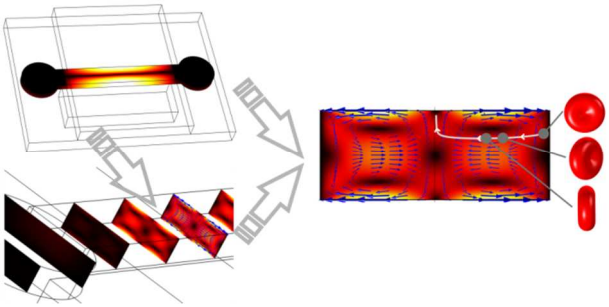

Journal Name

ARTICLE TYPE

Cite this: DOI: 10.1039/xxxxxxxxxx

Numerical simulation of acoustofluidic manipulation by radiation forces and acoustic streaming for complex particles†

Philipp Hahn,* Ivo Leibacher, Thierry Baasch, and Jurg Dual

Received Date
Accepted Date

DOI: 10.1039/xxxxxxxxxx

www.rsc.org/journalname

The numerical prediction of acoustofluidic particle motion is of great help for the design, the analysis, and the physical understanding of acoustofluidic devices as it allows for a simple and direct comparison with experimental observations. However, such a numerical setup requires detailed modeling of the acoustofluidic device with all its components and thorough understanding of the acoustofluidic forces inducing the particle motion. In this work, we present a 3D trajectory simulation setup that covers the full spectrum, comprising a time-harmonic device model, an acoustic streaming model of the fluid cavity, a radiation force simulation, and the calculation of the hydrodynamic drag. In order to make quantitatively accurate predictions of the device vibration and the acoustic field, we include the viscous boundary layer damping. Based on Nyborg's semi-analytical method, the boundary-driven acoustic streaming is derived directly from the device simulation and takes into account cavity wall vibrations which has often been neglected in the literature. The acoustic radiation forces and the hydrodynamic drag are calculated numerically to handle particles of arbitrary shape, structure, and size. In this way, complex 3D particle translation and rotation inside experimental micro-devices can be predicted. We simulate the rotation of a micro-fiber in an amplitude modulated 2D field and analyze the results with respect to experimental observations. For a quantitative verification, the motion of an alumina micro-disk is compared to a simple experiment. Demonstrating the potential of the simulation setup, we compute the trajectory of a red blood cell inside a realistic micro-device under the simultaneous effects of acoustic streaming and radiation forces.

1 Introduction

Ultrasonic standing waves inside the fluid cavity of acoustofluidic devices can be used to manipulate suspended micro-particles in a contactless fashion. There are two distinct acoustofluidic manipulation mechanisms: *acoustic radiation forces* allow to move particles relative to the surrounding fluid body; *acoustic streaming* allows to drag particles along with an acoustically induced fluid flow. Acoustofluidics offers an attractive alternative to technologies like hydrodynamic, dielectrophoretic, magnetophoretic, or optical particle manipulation.[1–4] In contrast to these technologies, it does not require specific electric, magnetic, or optical particle properties and it is known for excellent cell viability when processing living biological samples like cells, bacteria, or larger organisms.[5,6] Massively parallel particle manipulation can be achieved easily because the acoustofluidic force fields spread over the volume of the fluid cavity.[7,8] Utilizing a broad range of particle processing capabilities such as sorting, trapping, handling, and mixing,[9–12] a number of promising applications has been demonstrated during the past years.[13] Most of them are related to the miniaturization of process steps in the life sciences. Along with the miniaturization comes a drastic reduction of sample sizes and processing times, which could become key for the development of novel products such as medical diagnostic rapid tests. A comprehensive review of theoretical work, experimental setups as well as recent developments can be found in the book *Microscale Acoustofluidics*.[13]

During the past years, the capability of computing hardware and the user friendliness of available simulation software have evolved significantly. This continuing development favors numerical acoustofluidic simulations which have already become an integral tool for the development of new devices and the understanding of complex acoustofluidic phenomena. Nevertheless, numerical acoustofluidic simulations still heavily rely on simplifications of the governing equations. Without simplifications, sim-

Institute of Mechanical Systems (IMES), Department of Mechanical and Process Engineering, ETH Zurich, Tannenstrasse 3, CH-8092 Zurich, Switzerland. Tel: +41 44 633 9237; E-mail: hahnp@ethz.ch

† Electronic Supplementary Information (ESI) available: [Matlab code for the 3D trajectory simulation of a red blood cell as well as finite element models for the micro-device, the acoustic streaming, the radiation forces, and the hydrodynamic resistance. Experimental video footage]. See DOI: 10.1039/b000000x/

ulations would be prohibitively expensive even for simple 2D examples.[14] The main cause is the multi-scale nature of the involved fluid dynamic effects. Specifically, there is a time scale-difference between the ultrasonic cycle (often in the sub-μs-range), the transient or asymptotic device behavior (in the ms-range), and the particle motion (typically in the s-range). Further, there is a length scale-difference between the size of the device (in the mm or cm range), the micro-particles (usually $1-100\,\mu$m), and the viscous and thermal boundary layers (sub-μm). A perturbation approach that was already applied in early analytical studies[15] can resolve the time-scale related problems by splitting all fields into a time-harmonic and a time-averaged part.[16,17] Resolving both the micro-particles and the 3D device geometry in the same numerical mesh is usually computationally infeasible. During time-harmonic device simulations, the particles are typically neglected. This simplification is justified in most experimental conditions since the average particle concentration is usually very low. Avoiding the need to resolve the micro-particles in this way, realistic 3D micro-devices can be simulated at reasonable computational cost. Here, the boundary layers do not have to be resolved since they only affect the damping and thus the attainable amplitudes at resonance. By using semi-analytical damping expressions to emulate the boundary layer loss, Finite Element (FE) device models can be set up to quantitatively predict the time-harmonic device motion and the acoustic field in the bulk of the fluid cavity.[18,19] This simplified treatment of the viscous and thermal boundary layers can be employed as long as their characteristic thickness is much smaller than the fluid cavity dimensions.

The driving mechanisms of acoustic streaming in surface acoustic wave (SAW) devices and bulk acoustic wave (BAW) devices often differ. Both boundary driven streaming and attenuation driven streaming are relevant for SAW devices.[20] The viscous boundary layers at the fluid cavity walls cause boundary driven streaming and the small attenuation length causes attenuation driven streaming.[15,21] Compared to SAW devices, the attenuation length in typical BAW devices is much larger, causing the boundary driven streaming to dominate. The larger attenuation length is related to lower driving frequencies (typically around $500\,$kHz to $5\,$MHz for BAW devices and $10\,$MHz to $1\,$GHz for SAW devices).[13] Thus, bulk attenuation driven streaming can usually be neglected for BAW devices which are in the focus of the present work. To simulate streaming in the fluid cavity, the viscous boundary layers need to be resolved at very high numerical cost to perform a numerical streaming simulation.[22,23] Due to the immense numerical effort, it is currently not possible to use this method for the simulation of acoustic streaming inside a 3D device. However, if the fluid cavity has no sharp re-entrant tips or edges, there exists a semi-analytical way to compute the acoustic streaming based on the time-harmonic field of the device simulation mentioned above.[24–28] This method, based on calculations by Nyborg, completely avoids the need to resolve the viscous boundary layers. Even though we will point out the limitations of Nyborg's model, it is applied in this work to simulate the acoustic streaming field inside the 3D fluid cavity at relatively low numerical cost.

Along with the acoustic streaming and the hydrodynamic buoyancy force, the acoustic radiation force is the primary physical effect affecting the time-averaged particle motion. Many experimental setups are used to manipulate spherical particles that are much smaller than the acoustic wavelength. In this special case, the radiation forces can be calculated analytically whereas the viscous boundary layer surrounding the particle can often be neglected.[29–31] The modeling of non-spherical particles is more involved because it requires numerical treatment.[32–34] These numerical calculations are very versatile since particles can be non-spherical and non-homogeneous, consisting of multiple materials.[30,33] Even though it is possible to consider the viscous boundary layer around the particle in these simulations, we neglect its effect on the radiation force in the present work to avoid the numerical effort associated with the resolution of the thin boundary layers.

Secondary radiation forces, arising from the acoustic particle-particle or particle-wall interaction become relevant only at close proximity. For small spherical particles, they can be calculated analytically[35,36] and it is simple to implement the effect in a radiation force simulation by including a second particle or a reflecting wall in the computational domain.[32] For simplicity, we assume here that particles are sufficiently far apart from each other and cavity walls to neglect secondary radiation forces.

A numerical setup for the trajectory simulation of small spherical particles under the simultaneous effects of acoustic streaming and acoustic radiation forces is already available in the literature.[23,37] For micro-particles of varying size, it has been used to analyze their translatory motion in a 2D acoustic field. With our work, we take the first step toward full 3D simulations, predicting particle translation as well as rotation of non-spherical particles or non-homogeneous particles that may consist of multiple materials. Furthermore, we obtain the streaming field directly from the continuum mechanical simulation of a realistic device, considering the effects of both the acoustic field and the cavity wall vibration. This feature is considered important because it has been indicated that differing wall motion can lead to significantly different streaming fields inside the fluid cavity.[38]

Our simulation setup enables us to address a number of acoustofluidic applications that so far could not be analyzed by any other reported solution. These applications include the rotation of a micro glass fiber,[39,40] the manipulation of elongated bacteria (salmonella),[41] the pre-alignment and pre-orientation of red blood cells for flow cytometry[42] and the alignment of microdisks to design the mechanical properties of disk-reinforced composite materials.[34] After a detailed discussion of the numerical simulation setup in section 2, three of these applications are discussed in section 3.

2 Numerical model for the simulation of acoustofluidic particle motion

The trajectory simulation procedure consists of several steps, implemented by Comsol Multiphysics FE models and Matlab scripts. As the main result, the time evolution of the particle position and orientation is obtained whereas intermediate information such as *e.g.* the radiation forces or the streaming velocity along the particle path are accessible as well. The structure of the simu-

lation setup is depicted in Fig. 1. To give a brief overview, the

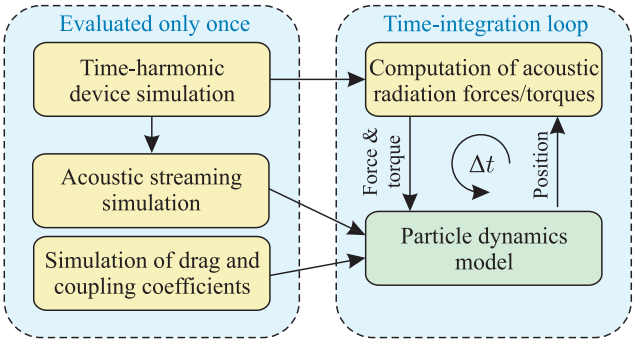

Fig. 1 Structure of the numerical setup for the simulation of 3D acoustophoretic particle motion. In a first step, the time-harmonic acoustic fields inside an acoustofluidic device are simulated. Based on the time-harmonic solution, the acoustic streaming field is computed inside the bulk of the fluid cavity. Also based on the device simulation, the acoustic radiation forces and torques on the particle are simulated at each time step. Both, streaming and radiation forces at the current particle position are necessary to determine the instantaneous particle velocity at each time step of the time-integration loop. The particle velocity can then be used to update the particle position. Prior to the trajectory simulation, the drag and coupling coefficients of the particle are taken from a hydro-dynamic simulation. The yellow boxes represent FE simulations done in Comsol whereas all other numerical calculations are implemented in Matlab.

main Matlab simulation script requires the hydrodynamic drag and coupling coefficients of the particle as input parameters and it establishes the connection to Comsol via the Comsol Livelink. In a first step, the script invokes the time-harmonic device simulation and the acoustic streaming simulation which is based on the latter. Subsequently, a numerical time stepping scheme is started to integrate the particle motion from the calculated particle velocity. At each time step, the radiation forces are computed and the stored streaming field is evaluated at the current location to update the particle velocity.

2.1 Time-harmonic device model

Acoustofluidic devices are usually composed of silicon, glass, or metal parts and a piezoelectric transducer. The FE device model solves the time-harmonic structural dynamic equations with electro-mechanical coupling for the piezoelectric material.[18,43] The indicial notation refers all quantities to an orthonormal basis with coordinates x_i; $i = 1,2,3$ whereas the derivative with respect to x_i is denoted by $_{,i}$. Furthermore, we will use Einstein's summation convention. It is understood that all fields are time-harmonic with the modulation factor $e^{\mathrm{i}\omega t}$ omitted for conciseness.[18] The first set of equations expresses the dynamic equilibrium,

$$\sigma_{ij,j} + \rho\omega^2 u_i = 0, \tag{1}$$

with the displacement field u_i, the stress field σ_{ij}, the material density ρ, and the angular frequency ω. The second set of equations enforces kinematic relations,

$$\gamma_{ij} = \frac{1}{2}\left(u_{i,j} + u_{j,i}\right), \tag{2}$$

with the strain field γ_{ij}. Furthermore, constitutive equations of all materials are required. Elastic materials show the functional relation $\sigma_\lambda = \sigma_\lambda(\gamma_\mu)$ with greek indices interpreted as double indices.[18,43] Piezoelectric materials show an additional dependence on the electric field E_k according to $\sigma_\lambda = \sigma_\lambda(\gamma_\mu, E_k)$.[18,44] Since BAW devices are operated in a resonant state to enhance the time-harmonic amplitudes and the related acoustofluidic forces, it is essential to implement material damping in the numerical model. The damping associated with solid elastic device components can be modeled by a complex stiffness tensor, whereas piezoelectric materials additionally require complex permittivity and piezoelectric coupling tensors.[18,44–46] For more details regarding the representation of solid elastic and piezoelectric materials, the reader is referred to Hahn et al.[18]

The fluid cavity is typically embedded in the solid device components and filled with the fluid-particle suspension. Since the particle concentration is usually very low (in the lower volume-‰ range), the governing equations for the fluid can be obtained from a first-order time-harmonic expansion of the Navier-Stokes equations.[16] Without resolving the details of the viscous boundary layer the equations can be simplified to the Helmholtz equation,

$$p_{,ii} = -k^2 p, \tag{3}$$

for the time-harmonic pressure field p whereas the wavenumber $k = \frac{2\pi}{\lambda} = \frac{\omega}{\bar{c}}$ is a function of either the acoustic wavelength λ or the angular frequency ω and the complex speed of sound $\bar{c}$. The time-harmonic velocity field v_i is calculated according to

$$v_i = \mathrm{i}\frac{1}{\rho_0\omega} p_{,i}, \tag{4}$$

with the quiescent fluid density ρ_0. The solid and fluid device components are coupled by fluid-structure interaction at the fluid cavity walls.[18,43] Damping due to the viscous and thermal dissipation in the bulk of the fluid and in the boundary layers at cavity walls and around suspended particles plays an important role by limiting the pressure amplitudes at resonance.[19] Thus, the damping limits the attainable acoustofluidic forces and it needs to be introduced in the device model by a complex speed of sound,

$$\bar{c}(f) = c_0\left(1 + \mathrm{i}\frac{\bar{\varphi}(f)}{2}\right), \tag{5}$$

where c_0 is the real-valued speed of sound in the fluid and the acoustofluidic loss factor $\bar{\varphi}(f)$ is derived from the acoustic mode shape inside the fluid cavity.[19] The above equations and the appropriate boundary conditions for the specific device are implemented by a Comsol multiphysics FE model.[18]

2.2 Acoustic streaming in the fluid cavity

As outlined above, it is prohibitively expensive to implement a 3D device model that resolves the viscous boundary layers in its computational mesh. However, the viscous boundary layers provide the main driving force for the streaming flow in the bulk of the fluid cavity.[25] A semi-analytic method for the simulation of acoustic streaming relies on calculations by Nyborg which were later extended for curved interfaces by Lee and Wang.[24–26] The

method requires knowledge of only the time-harmonic fields outside the boundary layers, thus avoiding the need to resolve them. The underlying idea is to use an analytical solution of the near boundary streaming at fluid-solid interfaces to come up with the streaming velocity just outside the near boundary streaming vortices. This velocity is called the *limiting velocity* and it serves as a boundary condition of a creeping flow simulation that reveals the streaming flow in the bulk of the fluid cavity. Analytical solutions of the near boundary streaming have been reported for flat and slightly curved interfaces. Herein, a major assumption is that the curvature radius of the fluid-solid interface is much larger than the thickness of the viscous boundary layer. On a planar interface that is normal to the inward pointing z-axis, the limiting velocity is computed from the time-harmonic velocity components u_{a0}, v_{a0} and w_{a0} in the two interface tangential directions x and y and the normal direction z, respectively.[25,26] The limiting velocity has a vanishing component in normal direction and the tangential components

$$u_{\mathrm{L}} = -\frac{1}{4\omega}\mathrm{Re}\Bigg\{ u_{\mathrm{a0}}\frac{u_{\mathrm{a0}}^*}{\mathrm{d}x} + v_{\mathrm{a0}}\frac{u_{\mathrm{a0}}^*}{\mathrm{d}y} + u_{\mathrm{a0}}^*\left[(2+\mathrm{i})\left(\frac{\mathrm{d}u_{\mathrm{a0}}}{\mathrm{d}x}+\frac{\mathrm{d}v_{\mathrm{a0}}}{\mathrm{d}y}+\frac{\mathrm{d}w_{\mathrm{a0}}}{\mathrm{d}z}\right)-(2+3\mathrm{i})\frac{\mathrm{d}w_{\mathrm{a0}}}{\mathrm{d}z}\right]\Bigg\}, \tag{6}$$

and

$$v_{\mathrm{L}} = -\frac{1}{4\omega}\mathrm{Re}\Bigg\{ u_{\mathrm{a0}}\frac{v_{\mathrm{a0}}^*}{\mathrm{d}x} + v_{\mathrm{a0}}\frac{v_{\mathrm{a0}}^*}{\mathrm{d}y} + v_{\mathrm{a0}}^*\left[(2+\mathrm{i})\left(\frac{\mathrm{d}u_{\mathrm{a0}}}{\mathrm{d}x}+\frac{\mathrm{d}v_{\mathrm{a0}}}{\mathrm{d}y}+\frac{\mathrm{d}w_{\mathrm{a0}}}{\mathrm{d}z}\right)-(2+3\mathrm{i})\frac{\mathrm{d}w_{\mathrm{a0}}}{\mathrm{d}z}\right]\Bigg\}, \tag{7}$$

where the asterisk denotes complex conjugation and $\mathrm{Re}\{X\}$ is the real part of X. The limiting velocity at curved interfaces is calculated in the same fashion with additional terms accounting for a curvilinear reference frame.[26] The method was successfully applied to analyze a complex streaming pattern in the transducer plane of a glass capillary device. Experimental Particle Image Velocimetry (PIV) measurements confirmed the numerically predicted streaming pattern.[27] Furthermore, a half-wavelength vortex pattern as observed in a multi-wavelength device could be explained.[28] In our implementation, we augment the device model of section 2.1 by an additional simulation step where the simulated time-harmonic velocities serve as the model input. Since the derivation of the limiting velocity method considers only the fluid velocity with no wall vibration in interface tangential direction, the expressions need to be modified slightly. Specifically, the time-harmonic interface tangential velocities u_{a0} and v_{a0} need to be calculated as the difference between the time-harmonic fluid velocity outside the boundary layer and the vibration velocities of the wall. They can be written as

$$u_{\mathrm{a0}} = v_x - \dot{u}_x, \quad \text{and} \quad v_{\mathrm{a0}} = v_y - \dot{u}_y, \tag{8}$$

where v_x and v_y are the tangential time-harmonic fluid velocity components, the dot denotes a time derivative, and the tangential wall displacement components are u_x and u_y. The latter can be found by a preceding time-harmonic device simulation as explained in section 2.1. The tangential relative velocities u_{a0} and v_{a0} cause a viscous boundary layer to form, which in turn causes the boundary driven acoustic streaming. No modification is required in interface normal direction. Here, the velocity component w_{a0} is identical to the fluid velocity component in normal direction v_z which in turn is equal to the wall velocity component in normal direction $\dot{u}_z$,

$$w_{\mathrm{a0}} = v_z = \dot{u}_z. \tag{9}$$

The major shortcoming of the method is that it cannot model the streaming around sharp re-entrant edges or tips. This problem is severe because it has been observed, that these geometric features can induce streaming velocities much higher than the ones induced by smooth walls.[47,48] For sharp tips and edges, there exists no analytic solution to draw on and it is questionable if a similar calculation procedure could be applied at all because the time-harmonic field and the streaming are not confined to a quasi 2D flow pattern as in the cases above. Furthermore, since the Helmholtz equation (eq. 3) is used to compute the time-harmonic fluid motion, the computed time-harmonic velocity becomes singular at re-entrant tips or edges. This means that the time-harmonic velocity field is not realistically modeled at these confined locations and even tends to infinity with successive mesh refinement. Due to the fact that the limiting velocity is computed from the simulated time-harmonic velocity at the fluid-solid interface, the deduced streaming field will show a strong disturbance at these locations. Even though such disturbances are observed experimentally, we emphasize that they cannot be modeled realistically by the limiting velocity method in its current form. Further work is necessary to develop a computationally efficient boundary-driven streaming model that can be applied for general devices with an arbitrary cavity geometry.

2.3 Acoustic radiation forces and torques on complex particles

As explained in section 1, acoustic scattering at a suspended particle influences the acoustic field in its vicinity but the global acoustic field inside the device is virtually unaffected if the particle concentration is low (in the order of 1‰ or less).[13] For this reason, the undisturbed acoustic field of the time-harmonic device simulation serves as the background field in a scattering simulation. Herein, the acoustic field in close proximity of the particle can be reconstructed. By modifying the numerical particle model, radiation forces can be computed for essentially any particle geometry, material, size, and structure. Based on the simulated field, composed of the background field and the scattering field, the radiation forces F_i^{rad} and torques T_i^{rad} can be calculated according to[32,49]

$$F_i^{\mathrm{rad}} = -\int_{S_0}\left[\left(\frac{1}{2\rho_0 c_0^2}\langle p^2\rangle - \frac{1}{2}\rho_0\langle v_j^2\rangle\right)n_i + \rho_0\langle (n_j v_j)v_i\rangle\right]\mathrm{d}S \tag{10}$$

and

$$T_i^{\mathrm{rad}} = -\int_{S_0} \epsilon_{ijk} r_j \left[\left(\frac{1}{2\rho_0 c_0^2} \langle p^2 \rangle - \frac{1}{2} \rho_0 \langle v_l^2 \rangle \right) n_k + \rho_0 \langle (n_l v_l) v_k \rangle \right] \mathrm{d}S, \tag{11}$$

where the integration is carried out over the particle surface S_0 but it could be any surface encompassing only the particle. The surface normal unit vector is n_j, ϵ_{ijk} is the Levi-Civita symbol and r_j is a vector, pointing from the center of the particle to the infinitesimal surface element $\mathrm{d}S$. The scattering simulation and the numerical surface integration are implemented in Comsol. The model consists of an acoustic domain for the fluid plus the particle representation which can be either modeled by a solid elastic domain, another acoustic domain or any combination of both, whichever best resembles the particle properties. Perfectly matched layers (PML) avoid backscattering at the domain boundaries to emulate the comparatively large fluid space surrounding the particle. The computational domain is depicted in Fig. 2. Effects like particle-particle or particle-wall interaction can be implemented by a second particle or reflective device walls in the computational domain. However, here we focus on situations where particles do not interact with each other or any device structure. Even though there is a complex dependence on the particle parameters, a separation distance longer than several particle dimensions is often sufficient to neglect interaction forces. This simplification can be made because the inter particle forces decay with the fourth power of the inter particle distance.[36]

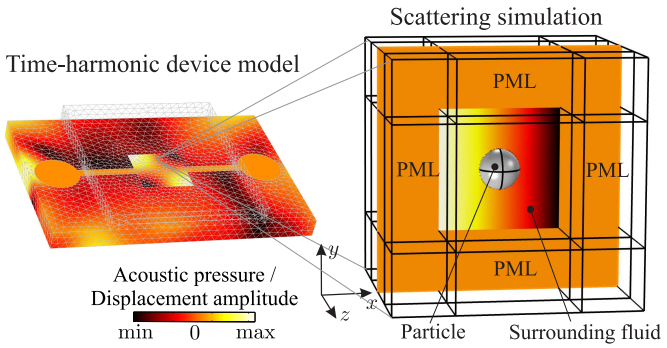

Fig. 2 3D Time-harmonic device simulation and computational domain of the particle scattering simulation to determine the acoustic radiation force and torque. The acoustic field of the scattering simulation is shown on one vertical cut-plane through the cubic domain. The acoustic background field in the vicinity of the particle is taken from the stored solution of the preceding device simulation. The time-harmonic particle displacement field and the acoustic field in the surrounding fluid are coupled by acoustic fluid-structure interaction whereas the particle model (a solid sphere in this case) can be as complicated as desired. An acoustic domain which is covered by perfectly matched layers (PML) models the fluid and minimizes the computational cost.

2.4 Time-averaged particle dynamics model

The dynamics of micro-particles in acoustofluidic devices is governed by a number of forces. In addition to the acoustic radiation forces and the buoyancy force, there exists a number of hydrodynamic forces that are hard to understand intuitively.[50,51] The most obvious force is the viscous drag due to the acoustic streaming field. However, there are also force effects arising from inertia and the simultaneous presence of a time-harmonic (acoustic) and a time-averaged (streaming) field. For example, in low frequency experiments at 1 kHz, it has been demonstrated that particle trapping can be achieved in an acoustic streaming vortex.[52] In the reported case, the particle dynamics is difficult to model.[51,53] We focus on typical bulk acoustic wave devices where the driving frequencies are often in excess of 1 MHz and the time-harmonic displacements are minute. In this case, it is possible to employ a number of approximations that simplify the particle dynamic equations dramatically. In essence, all inertial and hydrodynamic forces except the viscous drag due to acoustic streaming are dropped. This is common to many studies[23,47,54] as it provides a good first approximation for most experimental situations. Even though it has been shown that osmotically swollen red blood cells can be deformed by the radiation pressure,[55] we also assume that particles keep their shape. Summarizing the model assumptions, the particle does not deform under the radiation pressure and its trajectory is not affected by inertial effects. This results in a linear relation between the applied forces and the particle-fluid relative velocity. In contrast to most acoustofluidic particle trajectory simulations in the literature,[37,38,53,56] the present work is concerned with non-spherical particles. While the hydrodynamic drag on spherical particles can be covered by a single drag coefficient, a more complex representation is needed for particles of general shape. Utilizing the linear relation between the applied forces and the particle-fluid relative velocity, a matrix formulation maps the 3D acoustofluidic motion of general particles,[57,58]

$$\begin{bmatrix} \mathbf{F}^{\mathrm{rad}} \\ \mathbf{T}^{\mathrm{rad}} \end{bmatrix} + \begin{bmatrix} \mathbf{F}^{\mathrm{b}} \\ \mathbf{0} \end{bmatrix} = \mathbf{L} \left(\begin{bmatrix} \mathbf{u} \\ \boldsymbol{\omega} \end{bmatrix} - \begin{bmatrix} \mathbf{u}^{\mathrm{s}} \\ \boldsymbol{\omega}^{\mathrm{s}} \end{bmatrix} \right), \tag{12}$$

where the bold symbols denote 3×1 column vectors and the 6×6 drag coefficient matrix $\mathbf{L}$. The vectors $\mathbf{F}^{\mathrm{rad}}$ and $\mathbf{T}^{\mathrm{rad}}$ contain the radiation force and torque components as calculated by eqs. 10 and 11, the buoyancy force vector is $\mathbf{F}^{\mathrm{b}}$, the particle translational velocity is $\mathbf{u}$, its rotational velocity is $\boldsymbol{\omega}$, the translational streaming velocity is $\mathbf{u}^{\mathrm{s}}$, and the streaming vorticity is $\boldsymbol{\omega}^{\mathrm{s}}$. The streaming velocity and vorticity are evaluated at the particle center location whereas the length scale over which both quantities change is assumed to be much larger than the particle. Given the forces, the streaming velocity and drag coefficient matrix, the system is solved for the particle velocity. Subsequently, numerical time-integration is employed to update the particle position and orientation from the calculated velocity. In order to achieve high order accuracy at no additional simulation cost, we employ the fourth-order Adams-Bashforth multistep method.[59] In contrast to commonly used Runge-Kutta methods, velocities do not have to be calculated at intermediate steps. The required additional radiation force simulations would create a high computational overhead. Compared to the fourth-order Runge-Kutta integration, we save 75% of the computing time.

The drag coefficient matrix $\mathbf{L}$ contains hydrodynamic drag and

coupling parameters that relate the particle-fluid relative velocity to the applied forces and vice versa. To determine its 36 parameters for a given particle geometry, the creeping flow around the particle needs to be simulated for 6 linearly independent motions. The most obvious choice is to simulate particle translation and rotation for the three cartesian directions. Each creeping flow simulation reveals one column of the drag coefficient matrix as illustrated for the translation along the x-axis,

$$\begin{bmatrix}\mathbf{F}^{\mathrm{d}}\\ \mathbf{T}^{\mathrm{d}}\end{bmatrix} = -\mathbf{L}\begin{bmatrix}v^{\mathrm{p}}\\ 0\\ \vdots\\ 0\end{bmatrix} \quad \Rightarrow \quad \begin{bmatrix}L_{11}\\ \vdots\\ L_{61}\end{bmatrix} = -\frac{1}{v^{\mathrm{p}}}\begin{bmatrix}\mathbf{F}^{\mathrm{d}}\\ \mathbf{T}^{\mathrm{d}}\end{bmatrix}, \tag{13}$$

where v^{p} is the prescribed particle velocity and the column vectors $\mathbf{F}^{\mathrm{d}}$ and $\mathbf{T}^{\mathrm{d}}$ are the simulated drag forces and torques, respectively. In the creeping flow simulation, we solve the Stokes equations for an incompressible fluid without body forces according to,[57]

$$\begin{aligned}\eta v^{\mathrm{c}}_{i,jj} - p^{\mathrm{c}}_{,i} &= 0,\\ v^{\mathrm{c}}_{i,i} &= 0,\end{aligned} \tag{14}$$

where v^{c}_i is the creeping flow velocity, the hydrodynamic pressure is p^{c}, and η is the dynamic viscosity. To mimic a situation without particle-particle or particle-wall interaction, a fairly large fluid space around the particle is simulated. The boundary conditions are chosen such that the flow velocities decay to zero at the outer boundaries as seen in Fig. 3. The particle surface velocity is prescribed to create the desired relative translation or rotation whereas drag forces and torques are computed from the surface traction on the particle surface.

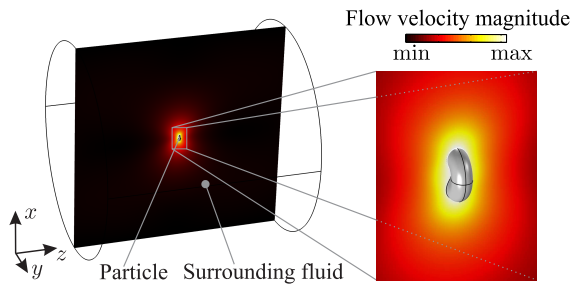

Fig. 3 FE simulation of the creeping flow due to the prescribed motion (here translation in x-direction) of a rigid micro-particle (here a red blood cell) in a large cylindrical fluid space with vanishing velocities at the outer boundaries. Shown is the velocity profile on the center x-z cut plane on the left hand side as well as a magnified view of the particle on the right hand side. Drag forces and torques are computed from the surface traction on the particle surface.

3 Simulation results and discussion

In the following three simulations we present applications of the presented trajectory simulation setup. Where possible, the comparison with experimental observations serves as a proof of concept for the numerical calculations. The capability of the simulation setup is showcased in three consecutive examples of increasing complexity. In the first two simulations, the acoustic field is prescribed analytically, eliminating many device-related effects for an easier interpretation. Since the particle manipulation in these examples is dominated by the acoustic radiation forces, acoustic streaming is neglected here. The first example analyzes a pure rotation of a glass micro-fiber, whereas the second example maps the simultaneous rotation and translation of an alumina micro-disk. While the first example only allows for a qualitative proof of concept, the second one allows for a quantitative comparison with experimental data. In order to showcase the full capability of the simulation setup, the motion of a human red blood cell (RBC) in a typical silicon-based micro-device is simulated. Here, the computations range from the time-harmonic device simulation, over the calculation of the acoustic streaming field inside the device, to the calculation of radiation forces and the integration of the translational and rotational particle motion. In general, it can be handy to simulate the particle motion first in an analytically prescribed acoustic field and without streaming, subsequently in the more realistic acoustic field of the device simulation (still without streaming), and finally in the realistic acoustic field and the streaming field from the device simulation. Even complex particle motion can be dissected in this way by linking different motion characteristics to the individual effects. The computations are performed on a desktop PC equipped with a quad-core Intel i7-2600K CPU, 32 GB RAM (DDR-3 1600 MHz) and Windows 7 (64-bit).

3.1 Rotation of a glass micro-fiber

In this first example, the rotation of a glass micro-fiber ($200\,\mu$m in length, $15\,\mu$m in diameter, density $2600\,\mathrm{kg/m^3}$, Young's modulus 73 GPa, Poisson's ratio 0.18) in a time-dependent acoustic field in water (speed of sound $1481\,\mathrm{m/s}$, density $998\,\mathrm{kg/m^3}$, dynamic viscosity $1\times10^{-3}\,\mathrm{Pa\,s}$, temperature $25\,^{\circ}\mathrm{C}$, frequency $1.09\,\mathrm{MHz}$) is simulated. In the experimental study, a silicon-based micro-device is used to separately excite two orthogonal standing waves in a quadratic fluid cavity, where the two modes are independently excited by orthogonal electrode strips on the piezoelectric transducer.[39,40] Amplitude modulation of the two excitation voltages creates a time-dependent acoustic field with a rotating line of zero pressure whereas the fiber is initially located in the rotation center at $x = y = 0$.[39] Analytically, the pressure field is given by

$$p = A_1\sin(kx) + A_2\sin(ky), \tag{15}$$

where A_1 and A_2 are the time-dependent amplitudes of the two orthogonal standing waves. Due to their high density, the fibers sediment and stay close to the cavity floor throughout the experiment. This avoids any rotation except the one in z-direction, perpendicular to the cavity floor. Therefore, in the simulation, the particle rotation along the x and y-axis are set to zero. Even though the drag coefficient matrix $\mathbf{L}$ of the fiber is likely to be affected by the presence of the cavity floor, we approximate it with the free space solution providing $L_{11} = 5.02\times10^{-7}\,\mathrm{Ns/m}$, $L_{22} = L_{33} = 6.25\times10^{-7}\,\mathrm{Ns/m}$, $L_{44} = 1.12\times10^{-16}\,\mathrm{Nms}$, $L_{55} = L_{66} = 3.52\times10^{-15}\,\mathrm{Nms}$. Due to symmetry, all other entries are zero whereas the values are given for a fiber pointing in x-

direction. In reality, we expect higher coefficients but we cannot quantify the difference due to lacking fiber-floor distance information. For instance, an assumed fiber-floor distance of 5μm roughly doubles the rotation drag coefficient L_{66} when compared to the the simulation without the floor.[40] In the computation of the radiation forces, both fiber ends have semi-spherical caps to avoid highly localized acoustic velocities which would require a very fine mesh. Resolving one fiber trajectory over a time range of 3 seconds in 400 integration steps took 6 hours of computing time. The simulation results confirm that the radiation forces tend to align the fiber (angle β) with the lines of zero pressure in the acoustic field (angle α) whereas simulated rotation speeds are in line with experimental observations (see Fig. 4). In the simulations, equal pressure amplitudes $A_1 = A_2 = 0.1$MPa are assumed for the orthogonal modes. The fiber follows the rotating lines of

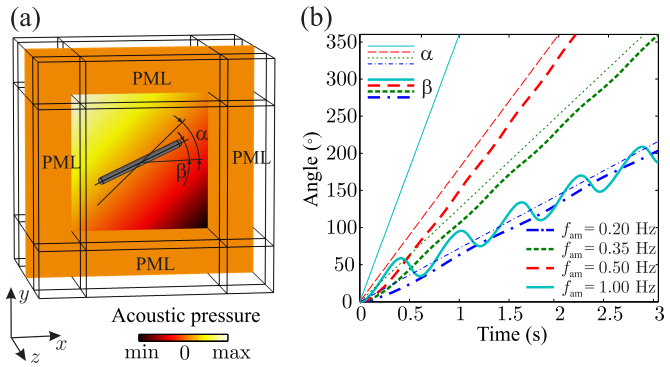

Fig. 4 (a) Glass micro-fiber inside the acoustic pressure field which rotates around the z-axis over time. The pressure field is generated by amplitude modulation of two orthogonal modes of equal maximum amplitude. Perfectly matched layers (PML) avoid reflections at the outer boundaries. (b) Orientation of the line of zero pressure α and the fiber axis β over time for different amplitude modulation frequencies f_{am}. In the initial configuration, α and β are both zero. As f_{am} is increased, the difference between α and β increases up to a point where the fiber cannot keep up any more. Once this limit is reached, the fiber is repeatedly overtaken by the faster rotating field, leading to a decreased mean rotation rate and a superimposed oscillatory component (see $f_{\mathrm{am}} = 1$Hz).

zero pressure but it lags behind due to the fluid dynamic resistance. If the acoustic field is rotated faster, the fiber rotation rate increases up to a limit where it cannot keep up any more. Above this limit, the fiber has a constant mean rotation rate and a superimposed oscillatory component (see $f_{\mathrm{am}} = 1$Hz). This stands in contrast to experiments where only the oscillatory part has been observed. However, there are usually amplitude differences between the two orthogonal standing waves which can explain this behavior. For an amplitude ratio of $A_1/A_2 = 0.8$ between the two standing waves, only the oscillatory component remains after the fiber has reached its mean orientation (see Fig. 5).

3.2 Trajectory of an alumina micro-disk in a 1D field

Another example for the acoustofluidic manipulation of non-spherical particles is the alignment of micro-platelets for the design of anisotropically platelet-reinforced composites.[60,61] Simple

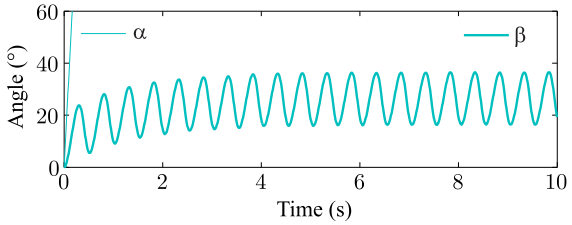

Fig. 5 Orientation of the line of zero pressure α and the fiber axis β over time for an amplitude modulation frequency $f_{\mathrm{am}} = 1$Hz and the amplitude A_1 of the standing wave in x-direction reduced by 20%. In the initial configuration, α and β are both zero. The angle α continues to grow linearly after leaving the plotted range. The fiber approaches a constant mean orientation and rotates in a purely oscillatory fashion (here at 2Hz which corresponds to twice the amplitude modulation frequency) as often observed in experiments.

acoustofluidic devices with a rectangular fluid channel were used to study the response of these platelets in a 1D standing wave.[34] For the simulation, the 1D standing wave is prescribed analytically by the pressure field

$$p = A\sin(kx), \tag{16}$$

where A is the pressure amplitude. Spherical micro-particles of similar size and of the same material migrate toward the pressure nodes of a standing wave. The same behavior can be expected from the micro-disks since the experimental manipulation frequencies are below the first structural disk resonance.[34] However, the disk shape adds a level of complexity that requires numerical modeling to predict the acoustofluidic disk motion consistent with experimental observations. In the experiments, it was demonstrated that the platelets rapidly align with the direction of the standing wave. The related rotation happens at a much faster pace than the translation toward the pressure nodal planes. The acoustophoretic platelet motion is well suited to validate our simulation setup as it allows the comparison of both rotation and translation at the same time. Given the experimental conditions, these two motion characteristics can be compared between the experiment and the simulation with only one fitting parameter which is the unknown time-harmonic pressure amplitude. In the experiment, the device is filled with a water-particle suspension containing less than 0.01 volume-% of alumina (Al_2O_3) micro-platelets to avoid particle-particle interaction as far as possible. The particle motion is captured by a high speed camera which is recording at 202 frames per second. A 1D standing wave in the rectangular cross section (width: 1500μm, depth: 140μm) of the fluid channel is excited at a frequency of 1.919MHz (2λ-mode). The particles are rather irregularly shaped platelets of varying size but they have a fairly constant thickness of 0.2μm. The acoustophoretic motion of one platelet was tracked with the video analysis software Xcitex ProAnalyst. This specific platelet is initially located very close to a pressure antinode (approximately 11μm apart). It was picked because it is clearly visible, it is almost shaped as a circular disk, it does not stick to the cavity floor, and it stays clear of other platelets until it reaches the agglomeration at the pressure node. Due to the acoustic radia-

tion forces, it is driven toward the pressure node and it aligns with the standing wave as shown in Fig. 6. During the experiments it became evident that particle sedimentation cannot be avoided even if the experiment was started immediately after the filling process. Therefore, it can be assumed that the platelet is initially very close to the cavity floor or even in contact with it. In the numerical trajectory simulation, we model the particle by a disk (thickness: 0.2μm, diameter: 12μm) whereas the diameter was deduced from the video footage. For this purpose, the video image was calibrated using a microfabricated calibration target to calculate the μm/pixel-ratio. The mechanical particle properties are: density $3900\,\mathrm{kg/m^3}$, Young's modulus $300\,\mathrm{GPa}$, and Poisson's ratio 0.222. The radiation forces and torques are calculated for an analytically prescribed 1D standing wave in water (speed of sound $1497\,\mathrm{m/s}$, density $997\,\mathrm{kg/m^3}$, dynamic viscosity $0.89\times10^{-3}\,\mathrm{Pa\,s}$, temperature $25\,^\circ\mathrm{C}$) whereas the pressure amplitude is fitted to match the translational motion of the experiment above. Because of the cavity geometry, the particle size, and the high acoustic contrast between the water and the particle material, the acoustic radiation forces are predominant. Therefore, acoustic streaming is neglected in the numerical simulation. For very small and dense particles like the disk in this experiment, it has been shown that the viscous and thermal boundary layers can significantly influence the acoustic radiation forces.[31,62] Therefore, the radiation forces in the experiment might differ from the simulated ones. Nevertheless, we believe that the differences are small enough that the particle motion is not affected in a qualitative sense and that the simulated inviscid radiation forces still provide a good first approximation. Similar as in the fiber rotation experiment of section 3.1, the drag coefficient matrix $\mathbf{L}$ of the disk is affected by the presence of the cavity floor. Nevertheless, we approximate it with the free space solution providing $L_{11}=8.21\times10^{-8}\,\mathrm{Ns/m}$, $L_{22}=L_{33}=5.82\times10^{-8}\,\mathrm{Ns/m}$, $L_{44}=2.16\times10^{-18}\,\mathrm{Nms}$, $L_{55}=L_{66}=1.93\times10^{-18}\,\mathrm{Nms}$. Due to symmetry, all other entries are zero whereas the values are given for a disk facing in x-direction. This rather crude approximation cannot be avoided since the particle-floor distance is unknown and it varies throughout the experiment. The simulation results corresponding to a time-harmonic pressure amplitude of $0.66\,\mathrm{MPa}$ (which is in a realistic experimental range[63]) are plotted in Fig. 7. As the main conclusion, we note that the high difference between translational and rotational motion is consistent with the experiments. Due to sedimentation, it can be assumed that the platelet is initially very close to the cavity floor or even in contact with it. This explains the delayed disk reorientation in the experiment. Compared to the simulation, the experimental rotation appears to be slightly faster, which can be attributed to the increasing radiation torque toward the pressure node.[34] At the instance of the rotation, the translation plots of Fig. 6 and 7 show a slight kink because of increased radiation forces in the final orientation. Sedimentation can explain why the kink is more clearly seen in the experimental data. In the initial orientation where the disk faces on the cavity floor, the drag enhancing effect of the floor is larger than in the rotated orientation where the particle stands upright on the floor. Finally, it is also interesting to note a slight acceleration followed by a slight backward motion between $0.78\,\mathrm{s}$ and $0.9\,\mathrm{s}$. Even though the video resolution is not high enough to rule out noise effects, it is clearly visible in

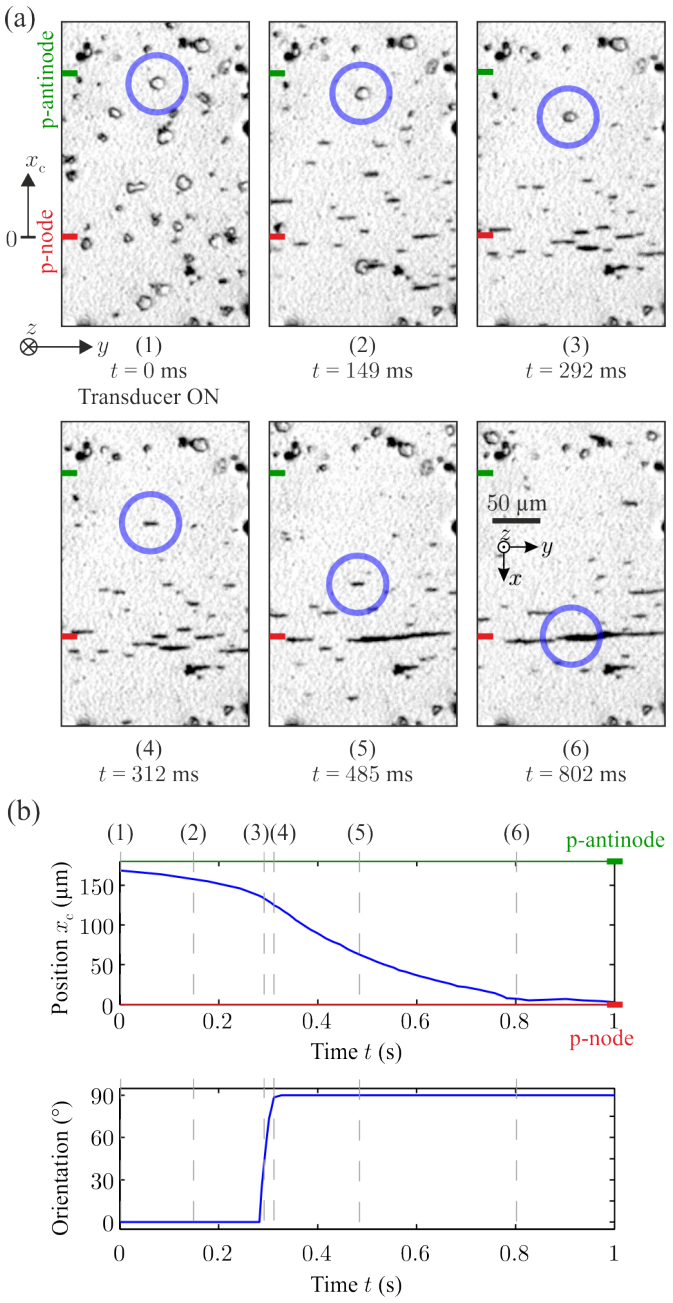

Fig. 6 Acoustophoresis of alumina micro-platelets in a 1D standing wave at $1.919\,\mathrm{MHz}$. (a) The image sequence shows the position and orientation of the analyzed particle (marked with a blue circle) at different time instances after activation of the ultrasonic field. This platelet is almost shaped as a circular disk and it stays well separated from other platelets until it reaches the agglomeration at the pressure node. As determined visually, the pressure nodal and the antinodal position are marked in red and green, respectively. (b) Particle center position x_c (in x-direction) and orientation (rotation angle around the y-axis, unknown rotation direction) as obtained from the video analysis. Dashed vertical lines mark the time instances corresponding to the video frames in (a). The position is measured from the pressure node and the orientation is derived from the projected particle surface on the view plane.

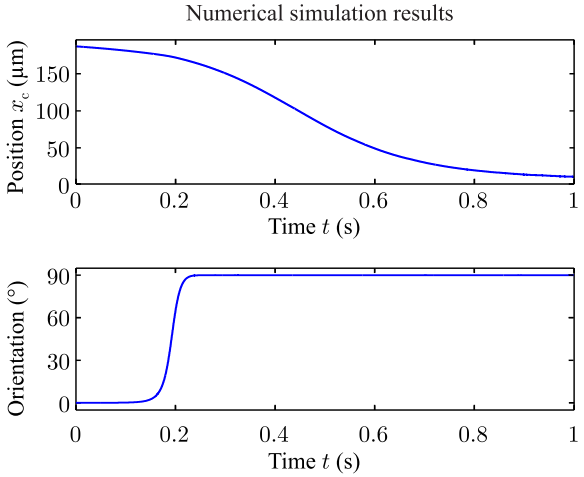

Fig. 7 Simulated motion of an alumina micro-disk in a $1.919\,\mathrm{MHz}$ 1D standing wave of pressure amplitude $0.66\,\mathrm{MPa}$. Starting at identical initial conditions as in the experiment ($11\,\mu\mathrm{m}$ apart from the pressure antinode corresponding to $x_c = 184\,\mu\mathrm{m}$ and facing in z-direction (see Fig. 6)), the particle center position and its orientation are plotted over the course of the simulation.

the video footage† that particle-particle interaction starts to take place at this point. In the simulation, the rotation direction is affected by numerical noise during the first integration steps and therefore random. In the experiment, we cannot tell the rotation direction due to the limited magnification of the video. Simulating the disk trajectory over a time range of 1 second in 4000 steps took 45 hours of computing time. The high number of integration steps becomes necessary because the rotational dynamics is much faster than the translational dynamics. In addition, each radiation force simulation is relatively expensive because the extremely high disk aspect ratio requires fine discretization.

3.3 Trajectory of a red blood cell in a realistic micro-device

Motivated by the application of acoustofluidic pre-alignment and pre-orientation for flow cytometry,[42] we simulate the motion of a red blood cell (RBC) in a simple micro-device. From a simulation point of view, this application is especially challenging because the acoustic radiation forces, the acoustic radiation torques, the translational acoustic streaming field and the streaming vorticity simultaneously affect the particle motion. To provide the complete picture, we obtain the time-harmonic field and the acoustic streaming field from a numerical device simulation as outlined in section 2. The example demonstrates the potential of our trajectory simulation setup as none of the simulation setups reported in the literature would be able to predict the complex particle motion in such a situation. The complete trajectory simulation setup comprising the device model, the streaming model, the particle drag computation, and radiation force simulation is provided in the Electronic Supplementary Information.† The piezoelectric device excitation at $1.44\,\mathrm{MHz}$ and $5\,\mathrm{Vpp}$ creates a strong half-wave resonance in the fluid channel of rectangular cross section ($500\,\mu\mathrm{m}$ in width, $200\,\mu\mathrm{m}$ in depth) as shown in Fig. 8 (a). In the simulation, it is assumed that there are no anchor losses into the device support. Experimental measurements have shown that this assumption holds if the device is placed on a soft support made of foam or tissue paper.[19] In many experiments, devices are clamped or glued to a device holder. In these cases, the attainable time-harmonic amplitudes are often reduced significantly and the modeling becomes more involved. The 3D streaming simulation results display the well-known Rayleigh streaming vortices of decreasing flow rates toward the open fluid reservoirs (see Fig. 8 (b)). The geometry of the human RBC ($3\,\mu\mathrm{m}$ in thickness, $8\,\mu\mathrm{m}$ in diameter)[64] is approximated by a Cassinian Oval.[65] Initially, it is located at $x = 0.24\,\mathrm{mm}$ and $z = -0.05\,\mathrm{mm}$ on the center x-z plane of the device where the time-harmonic field is maximum and its rotational symmetry axis points in y-direction (see Fig. 9 (a)). In the calculation of the radiation forces and torques, the RBC is modeled by an acoustic domain

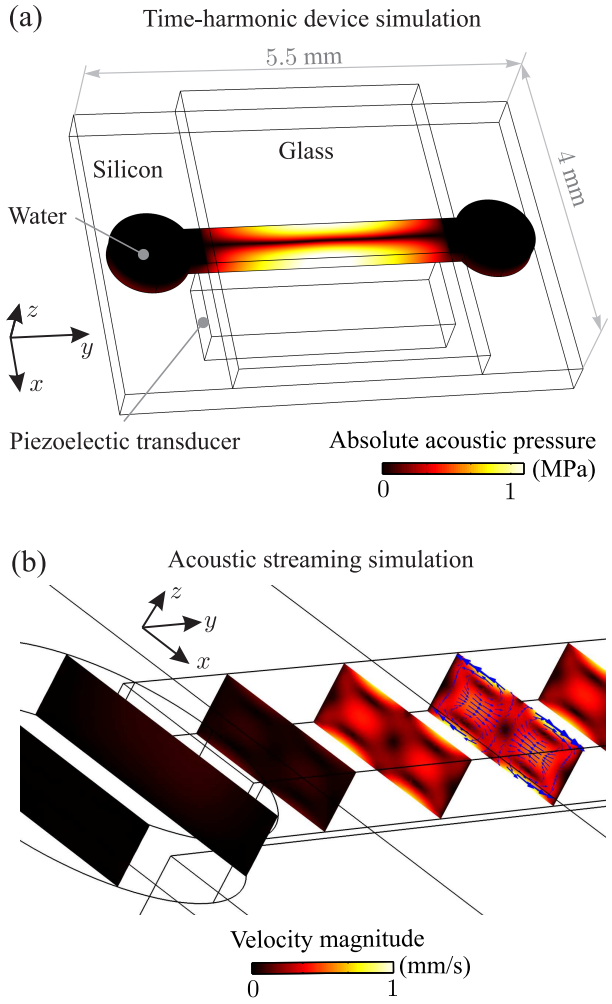

Fig. 8 (a) Time-harmonic simulation of the coupled solid device components and the fluid. At $1.44\,\mathrm{MHz}$, a half-wave resonance develops in the x-direction of the fluid channel which has open reservoirs at both ends. (b) 3D acoustic streaming flow, obtained by the limiting velocity method for the computed half-wave resonance in the fluid channel. The magnitude of the streaming velocity is shown on x-z cut planes whereas the highest values are reached in the center cut plane, coinciding with maximum time-harmonic pressure.

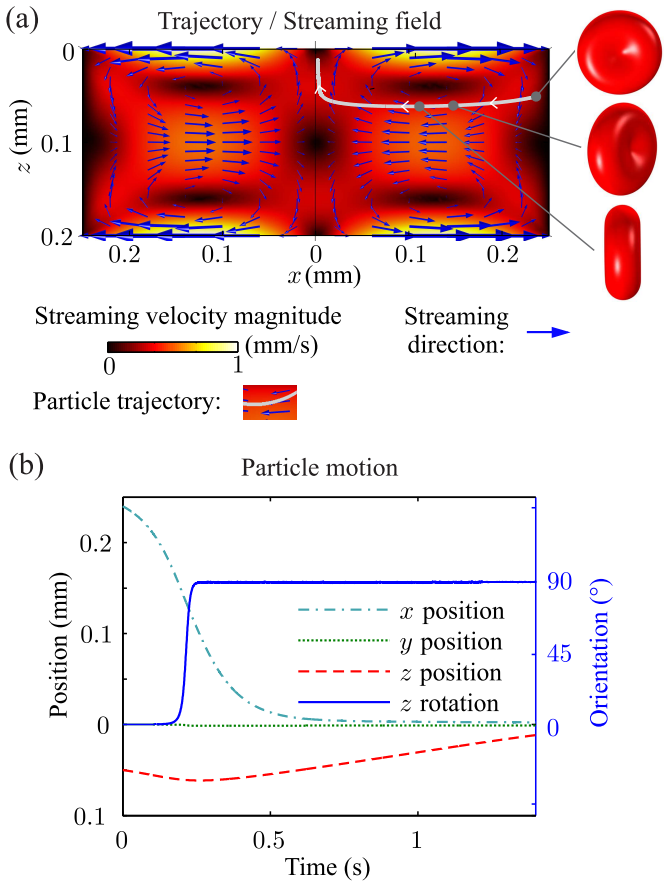

Fig. 9 (a) Trajectory of the RBC due to acoustic radiation forces and acoustic streaming. The velocity magnitude and the direction of the streaming profile in the center x-z cut plane of the fluid channel are shown in the background. On the right hand side, the orientation of the RBC is given at three time instances. (b) Time evolution of the RBC center position and rotation angle around the z-axis. The motion in x-direction can mainly be attributed to the radiation force while the motion in z-direction is caused by acoustic streaming.

of density $1139\,\mathrm{kg/m^3}$ and speed of sound $1680\,\mathrm{m/s}$.[55] The water properties are chosen as specified in section 3.2. For the simulated resonance mode in the device, the acoustofluidic loss factor calculation yields $\bar{\varphi} = 2.31 \times 10^{-3}$.[19] All model details and material parameters can be found in the Comsol FE model.† Even though it has been shown that RBCs can be deformed by the acoustic radiation pressure,[55] we neglect their time-averaged deformation since the applied radiation pressure is about five times smaller in our case. Simulating the RBC drag coefficient matrix $\mathbf{L}$ yields $L_{11} = 6.15 \times 10^{-8}\,\mathrm{Ns/m}$, $L_{22} = L_{33} = 5.46 \times 10^{-8}\,\mathrm{Ns/m}$, $L_{44} = 1.03 \times 10^{-18}\,\mathrm{Nms}$, $L_{55} = L_{66} = 8.14 \times 10^{-19}\,\mathrm{Nms}$. Due to symmetry, all other entries are zero whereas the rotational symmetry axis of the RBS points in x-direction. The trajectory is simulated over a range of $1.4\,\mathrm{s}$ with the results illustrated in Fig. 9. The radiation force acts in negative x-direction and causes the particle to move toward the pressure node at $x = 0$. During the first $0.5\,\mathrm{s}$, the velocity component induced by radiation forces is higher than the streaming velocity. Nevertheless, the deflection due to the streaming field in z-direction is clearly visible and even becomes dominant once the particle approaches $x = 0$. As observed in experiments, the radiation torque tends to align the RBC symmetry axis with the normal vector of the constant time-harmonic pressure planes.[42] After around $0.2\,\mathrm{s}$, the RBC rotates rapidly around the z-axis by an angle of $90°$. The whole simulation took 60 hours of computing time.

4 Conclusions

Numerical trajectory simulation is ideally suited to analyze acoustofluidic devices because it allows a direct and straight forward comparison with experimental observations. Furthermore, it provides profound insight in the underlying physical effects with implications on future device designs. We have presented a comprehensive numerical setup for the simulation of 3D acoustofluidic particle motion. It is designed to handle arbitrary particles and it is able to resolve their translational and rotational dynamics under challenging conditions where acoustic radiation forces and boundary-driven acoustic streaming act simultaneously. For the proof of concept, we have simulated the acoustophoretic motion of a micro-fiber and a micro-disk. The simulation results are both qualitatively and quantitatively in line with the experimental data. Further, we were able to explain complex phenomena related to the acoustofluidic rotation of a micro-fiber at high rotation rates and the speed difference between the translational and rotational dynamics of oblate particles. Demonstrating the full capability of the simulation setup, we predict the motion of a red blood cell inside a realistic micro-device. To date, the computational costs are relatively high but they could be reduced by a more sophisticated time integration scheme with variable step width. A real limitation, however, represents the limiting velocity streaming simulation which is currently only applicable to geometrically simple fluid cavities. A more general, yet computationally feasible solution to this problem would further increase the number of potential applications for our simulation model. As the main result of this work, we provide the full simulation setup in the Electronic Supplementary Information.† It can be used to analyze a wide range of experimental setups. Additionally, there is the option to include additional effects and refinements like particle-particle or particle-wall interactions. In this way, another field of attractive applications can be analyzed numerically.

References

1 A. Karimi, S. Yazdi and A. Ardekani, *Biomicrofluidics*, 2013, **7**, 021501.
2 R. Pethig, *Biomicrofluidics*, 2010, **4**, 022811.
3 M. Zborowski and J. J. Chalmers, in *Magnetophoresis: Fundamentals and Applications*, John Wiley & Sons, 1999.
4 D. G. Grier, *Nature*, 2003, **424**, 810–816.
5 M. Wiklund, *Lab Chip*, 2012, **12**, 2018–2028.
6 X. Ding, S.-C. S. Lin, B. Kiraly, H. Yue, S. Li, I.-K. Chiang, J. Shi, S. J. Benkovic and T. J. Huang, *Proc. Natl. Acad. Sci. U.S.A.*, 2012, **109**, 11105–11109.
7 T. Laurell, F. Petersson and A. Nilsson, *Chem. Soc. Rev.*, 2007, **36**, 492–506.

8 F. J. Trujillo, S. Eberhardt, D. Möller, J. Dual and K. Knoerzer, *Ultrason. Sonochem.*, 2013, **20**, 655 – 666.

9 P. Augustsson, C. Magnusson, M. Nordin, H. Lilja and T. Laurell, *Anal. Chem.*, 2012, **84**, 7954–7962.

10 S. Li, P. Glynne-Jones, O. Andriotis, K. Ching, U. Jonnalagadda, R. Oreffo, M. Hill and R. Tare, *Lab Chip*, 2014, **14**, 4475.

11 A. E. Christakou, M. Ohlin, B. Vanherberghen, M. A. Khorshidi, N. Kadri, T. Frisk, M. Wiklund and B. Önfelt, *Integr. Biol.*, 2013, **5**, 712–719.

12 P.-H. Huang, Y. Xie, D. Ahmed, J. Rufo, N. Nama, Y. Chen, C. Y. Chan and T. J. Huang, *Lab Chip*, 2013, **13**, 3847–3852.

13 *Microscale Acoustofluidics*, ed. T. Laurell and A. Lenshof, Royal Society of Chemistry, Cambridge, UK, 2015.

14 J. Wang and J. Dual, *J. Phys. A: Math. Theor.*, 2009, **42**, 285502.

15 L. Rayleigh, *Philos. Trans. R. Soc. London*, 1884, **175**, 1–21.

16 H. Bruus, *Lab Chip*, 2012, **12**, 20–28.

17 H. Bruus, *Lab Chip*, 2012, **12**, 1014–1021.

18 P. Hahn, O. Schwab and J. Dual, *Lab Chip*, 2014, **14**, 3937–3948.

19 P. Hahn and J. Dual, *Phys. Fluids*, 2015, **27**, 062005.

20 M. Wiklund, R. Green and M. Ohlin, *Lab Chip*, 2012, **12**, 2438–2451.

21 C. Eckart, *Phys. Rev.*, 1948, **73**, 68–76.

22 P. B. Muller and H. Bruus, *Phys. Rev. E*, 2014, **90**, 043016.

23 P. B. Muller, M. Rossi, A. G. Marin, R. Barnkob, P. Augustsson, T. Laurell, C. J. Kähler and H. Bruus, *Phys. Rev. E*, 2013, **88**, 023006.

24 W. L. Nyborg, *J. Acoust. Soc. Am.*, 1953, **25**, 68–75.

25 W. L. Nyborg, *J. Acoust. Soc. Am.*, 1958, **30**, 329–339.

26 C. P. Lee and T. G. Wang, *J. Acoust. Soc. Am.*, 1989, **85**, 1081–1088.

27 J. Lei, P. Glynne-Jones and M. Hill, *Lab Chip*, 2013, **13**, 2133–2143.

28 J. Lei, M. Hill and P. Glynne-Jones, *Lab Chip*, 2014, **14**, 532–541.

29 L. P. Gor'kov, *Sov. Phys. Dokl. (Engl. Transl.)*, 1962, **6**, 773–775.

30 I. Leibacher, W. Dietze, P. Hahn, J. Wang, S. Schmitt and J. Dual, *Microfl. Nanofl.*, 2014, **16**, 513–524.

31 M. Settnes and H. Bruus, *Phys. Rev. E*, 2012, **85**, 016327.

32 J. Dual, P. Hahn, I. Leibacher, D. Moller, T. Schwarz and J. Wang, *Lab Chip*, 2012, **12**, 4010–4021.

33 P. Glynne-Jones, P. P. Mishra, R. J. Boltryk and M. Hill, *J. Acoust. Soc. Am.*, 2013, **133**, 1885–1893.

34 A. Garbin, I. Leibacher, P. Hahn, H. LeFerrand, A. Studart and J. Dual, *submitted to J. Acoust. Soc. Am.*, 2015.

35 J. Wang and J. Dual, *Ultrasonics*, 2012, **52**, 325–332.

36 G. T. Silva and H. Bruus, *Phys. Rev. E*, 2014, **90**, 063007.

37 P. B. Muller, R. Barnkob, M. J. H. Jensen and H. Bruus, *Lab Chip*, 2012, **12**, 4617–4627.

38 M. Antfolk, P. B. Muller, P. Augustsson, H. Bruus and T. Laurell, *Lab Chip*, 2014, **14**, 2791–2799.

39 T. Schwarz, G. Petit-Pierre and J. Dual, *J. Acoust. Soc. Am.*, 2013, **133**, 1260–1668.

40 T. Schwarz, P. Hahn, G. Petit-Pierre and J. Dual, *Microfl. Nanofl.*, 2015, **18**, 65–79.

41 T. Schwarz and J. Dual, *AIP Conference Proceedings*, 2012, **1433**, 779–782.

42 O. Jakobsson, M. Antfolk and T. Laurell, *Anal. Chem.*, 2014, **86**, 6111–6114.

43 J. Dual and T. Schwarz, *Lab Chip*, 2012, **12**, 244–252.

44 J. Dual and D. Moller, *Lab Chip*, 2012, **12**, 506–514.

45 L. E. Kinsler, A. R. Frey, A. B. Coppens and J. V. Sanders, *Fundamentals of Acoustics*, Wiley, New York, 2nd edn., 2000.

46 S. Sherrit and B. K. Mukherjee, in *Characterization of Piezoelectric Materials for Transducers*, Research Signpost, Kerala, India, 2012, pp. 185–254.

47 N. Nama, P.-H. Huang, T. J. Huang and F. Costanzo, *Lab Chip*, 2014, **14**, 2824–2836.

48 I. Leibacher, P. Hahn and J. Dual, *Microfl. Nanofl.*, 2015.

49 K. Yosioka, Y. Kawasima and H. Hirano, *Acta Acust. united with Acust.*, 1955, **5**, 173–178.

50 M. R. Maxey and J. J. Riley, *Phys. Fluids*, 1983, **26**, 883–889.

51 K. Chong, S. D. Kelly, S. Smith and J. D. Eldredge, *Phys. Fluids*, 2013, **25**, 033602.

52 B. R. Lutz, J. Chen and D. T. Schwartz, *Anal. Chem.*, 2006, **78**, 5429–5435.

53 P. Agrawal, P. S. Gandhi and A. Neild, *Phys. Rev. Applied*, 2014, **2**, 064008.

54 H. Bruus, *Lab Chip*, 2012, **12**, 1578–1586.

55 P. Mishra, M. Hill and P. Glynne-Jones, *Biomicrofluidics*, 2014, **8**, 034109.

56 N. Nama, R. Barnkob, Z. Mao, C. J. Kahler, F. Costanzo and T. J. Huang, *Lab Chip*, 2015, **15**, 2700–2709.

57 J. Happel and H. Brenner, *Low Reynolds number hydrodynamics*, Martinus Nijhoff, 1983.

58 O. Gonzalez, A. Graf and J. Maddocks, *J. Fluid Mech.*, 2004, **519**, 133–160.

59 J. C. Butcher, *J. Comp. Appl. Math.*, 2000, **125**, 1–29.

60 R. M. Erb, R. Libanori, N. Rothfuchs and A. R. Studart, *Science*, 2012, **335**, 199–204.

61 R. M. Erb, J. Segmehl, M. Schaffner and A. R. Studart, *Soft Matter*, 2013, **9**, 498–505.

62 J. T. Karlsen and H. Bruus, *arXiv preprint arXiv:1507.01043*, 2015.

63 R. Barnkob, P. Augustsson, T. Laurell and H. Bruus, *Lab Chip*, 2010, **10**, 563–570.

64 E. Evans and Y.-C. Fung, *Microvascular research*, 1972, **4**, 335–347.

65 B. ANGELOV and I. M. MLADENOV, Proc. of Geometry, Integrability and Quantization, Varna, Bulgaria, 1999, pp. 27–46.